

Time-Dependent Optical Spectroscopy of GRB 010222: Clues to the GRB Environment¹

N. Mirabal², J. P. Halpern², S. R. Kulkarni³, S. Castro^{3,4}, J. S. Bloom³, S. G. Djorgovski³, T. J. Galama³, F. A. Harrison³, D. A. Frail⁶, P. A. Price³, D. E. Reichart³ and H. Ebeling⁵

ABSTRACT

We present sequential optical spectra of the afterglow of GRB 010222 obtained one day apart using the Low Resolution Imaging Spectrometer (LRIS) and the Echellette Spectrograph and Imager (ESI) on the Keck telescopes. Three low-ionization absorption systems are spectroscopically identified at $z_1 = 1.47688$, $z_2 = 1.15628$, and $z_3 = 0.92747$. The higher resolution ESI spectrum reveals two distinct components in the highest redshift system at $z_{1a} = 1.47590$ and $z_{1b} = 1.47688$. We interpret the $z_{1b} = 1.47688$ system as an absorption feature of the disk of the host galaxy of GRB 010222. The best fitted power-law optical continuum and [Zn/Cr] ratio imply low dust content or a local gray dust component near the burst site. In addition, we do not detect strong signatures of vibrationally excited states of H_2 . If the GRB took place in a superbubble or young stellar cluster, there are no outstanding signatures of an ionized absorber, either. Analysis of the spectral time dependence at low resolution shows no significant evidence for absorption-line variability. This lack of variability is confronted with time-dependent photoionization simulations designed to apply the observed flux from GRB 010222 to a variety of assumed atomic gas densities and cloud radii. The absence of time dependence in the absorption lines implies that high-density environments are disfavored. In particular, if the GRB environment was dust

¹Based on data obtained at the W.M. Keck Observatory, which is operated as a scientific partnership among the California Institute of Technology, the University of California, and NASA, and was made possible with the generous financial support of the W.M. Keck Foundation

²Astronomy Department, Columbia University, 550 West 120th Street, New York, NY 10027

³California Institute of Technology, Palomar Observatory 105-24, Pasadena, CA 91125

⁴Infrared Processing and Analysis Center, 100-22 California Institute of Technology, 105-24, Pasadena, CA 91125

⁵Institute for Astronomy, University of Hawaii, 2680 Woodlawn Drive, Honolulu, HI 96822

⁶National Radio Astronomy Observatory, Socorro, NM 87801

free, its density was unlikely to exceed $n_H = 10^2 \text{ cm}^{-3}$. If depletion of metals onto dust is similar to Galactic values or less than solar abundances are present, then $n_H \geq 2 \times 10^4 \text{ cm}^{-3}$ is probably ruled out in the immediate vicinity of the burst.

Subject headings: Gamma rays: Bursts — Cosmology: Observations — Galaxies: abundances, ISM, star clusters

1. Introduction

Years after the serendipitous discovery of gamma-ray bursts (GRBs) by the Vela spacecraft (Klebesadel et al. 1973), the nature of the progenitors responsible for generating the initial explosion remains uncertain, while an elegant set of ideas about the production and evolution of the afterglow has developed (Mészáros & Rees 1997; Sari & Piran 1997).

Aside from recent breakthroughs in X-ray spectroscopy of GRBs (*e.g.*, Piro et al. 2000) a large fraction of the observational information about the environments of GRBs derives from optical spectroscopy and imaging of the host galaxies. Optical spectroscopy of the integrated light and calibrated emission lines has been used to derive the star-formation rate (SFR) for a number of the host galaxies (see for instance Bloom et al. 1998; Djorgovski et al. 1998). As a complement to spectroscopy, high-resolution optical imaging and astrometry have helped pinpoint two-dimensional locations for GRBs with respect to the host galaxy. The distribution of these GRB locations has yielded a number of statistical constraints in the progenitor scenarios (*e.g.*, Bloom, Kulkarni, & Djorgovski 2000).

A promising technique that has been applied with less success so far is the study of time dependence in absorption lines from metal ions (Perna & Loeb 1998; Böttcher et al. 1999) or H_2 vibrational levels (Draine 2000) that might be excited by the UV radiation generated during the evolution of the burst. The detection of absorption-line variability could provide important clues about the physical dimensions of the photoionized region and the density in the immediate environment of the GRB. Absorption-line variability can be quantified by measuring changes in the equivalent widths as a function of time or by identifying the appearance of new absorption features. Vreeswijk et al. (2001) studied the time evolution of the Mg II doublet in the optical spectra of GRB 990510 and GRB 990712 but failed to find any significant changes. In this work we present a study of the time evolution of absorption systems in the optical spectrum of GRB 010222, and discuss possible implications for its progenitor environment. The outline of the paper is as follows: §2 describes the optical spectroscopy, §3 describes the absorption line identification and continuum fitting. In §4

we detail column density determinations, arguments in favor of the $z = 1.47688$ redshift for GRB 010222, kinematics of the host galaxy, and a study of time evolution of absorption lines. A description of the photoionization code and results is given in §5 and §6. Finally, the implications of our results and conclusions are presented in §7 and §8.

2. Observations

2.1. LRIS Spectroscopy

GRB 010222 was initially detected by BeppoSAX on UT 2001 Feb. 22.30799 (Piro 2001). An optical counterpart was reported only a few hours later by Henden (2001a,2001b). Our group began spectroscopic observations at the position of the optical counterpart on UT 2001 February 22.66 with the dual-beam Low Resolution Imaging Spectrometer (LRIS) on the Keck I telescope and obtained a second spectrum on UT 2001 February 23.66. On both nights we used a 300 lines/mm grating blazed at 5000 Å with a 1".5 wide slit. The effective spectral resolution FWHM varies from ≈ 13 Å on the blue side to ≈ 11 Å on the red side. A total of 1800 s of exposure were obtained on each night. The data were trimmed, bias-subtracted and flat-fielded using standard procedures. Extraction of the spectra was performed using the IRAF APALL package. Telluric lines were corrected by fitting the continuum including the A and B atmospheric bands of a spectrophotometric standard. The spectra of spectrophotometric standards Feige 67, Hiltner 600, and HZ 44 were used for flux calibration and a Hg-Kr-Ne-Ar-Xe comparison lamp provided the wavelength calibration. The wavelength calibrations have a typical accuracy of $\approx 0.2 - 0.5$ Å as determined by the root-mean-square (rms) deviation of the individual lines from the smooth function used to fit them. The large range of precision reflects the presence of fewer arc lines on the blue side. Finally, the LRIS-B (blue channel) and LRIS-R (red channel) spectra were connected at the crossover wavelength of the dichroic beam splitter.

2.2. ESI Spectroscopy

A higher-resolution spectrum of GRB 010222 was obtained on UT 2001 Feb 23.61 using the Echellette Spectrograph and Imager (ESI) mounted on the Keck II telescope. This mode spans ten orders with effective wavelength coverage from 3900 Å to 10900 Å. The spectral resolution is $11.4 \text{ km s}^{-1} \text{ pix}^{-1}$ with typical dispersion in the instrument ranging from $0.16 \text{ Å pixel}^{-1}$ in order 15 to $0.30 \text{ Å pixel}^{-1}$ in order 6. In the echellette mode the instrument provides a wavelength resolution $R \approx 10000$ over the entire spectrum. A total of 3×1200

second exposures were obtained and reduced using Tom Barlow’s Mauna Kea Echelle Extraction program (MAKEE)⁷. MAKEE, originally designed for the High Resolution Echelle Spectrometer (HIRES), is an automated procedure that allows standard processing as well as wavelength and flux normalization. For the wavelength calibration we used a CuAr cathode lamp which provides a large number of unsaturated lines to fit the spectrum with rms $\approx 0.09 \text{ \AA}$. The individual spectra at a common epoch were average-combined after running through the pipeline extraction.

3. Reductions

3.1. Absorption System Identifications

We have identified three absorption systems (Bloom et al. 2001; Castro et al. 2001a) which were reported independently by Jha et al. (2001). The systems are located at $z_1 = 1.47688$, $z_2 = 1.15628$, and $z_3 = 0.92747$, where the redshift reported is the average of individual lines for each system. The line identification corresponds to a cross-correlation of features in the spectrum with a listing of known absorption lines (Verner, Barthel, & Tytler 1994) assuming possible redshift systems at z_1 , z_2 , and z_3 . In order to weed out spurious features possibly due to sky subtraction, only those lines present in three spectra are reported. Moreover, we demanded $\lambda_{rest}[1.0 + z(1-x)] < \lambda_{obs} < \lambda_{rest}[1.0 + z(1+x)]$ and the corresponding oscillator strength ratios for identified lines. In the previous, x stands for a tolerance factor in the line identification and accounts for uncertainties in the wavelength calibration. Figure 1 shows the LRIS spectra including line identification for each absorption system. The higher-resolution ESI spectrum with identified absorption features is shown in Figure 2. In the highest redshift system we find kinematic evidence for two distinct components at $z_{1a}=1.47590$ and $z_{1b}=1.47688$ respectively, with a rest-frame separation of $\approx 119 \text{ km s}^{-1}$. The kinematic structure of this system will be discussed at greater length in §4.3. Tables 1 and 2 summarize the line identifications for each setup and list the measured vacuum wavelengths, observed wavelengths converted into vacuum and corrected for heliocentric motion, estimated redshift, oscillator strengths f_{ij} , equivalent widths (W_o) in the rest frame for both nights, and error estimates in their equivalent widths. We have adopted the compilation of wavelengths and oscillator strengths by Morton (1991) with the revisions proposed by Savage & Sembach (1996). The main source of uncertainty in the equivalent width measurements derives from the identification of the continuum level. In order to compute the errors in the equivalent width for each line we used the IRAF SPLIT task which allows error estimates

⁷See <http://spider.ipac.caltech.edu/staff/tab/makee/>

based on a Poisson model for the noise. For blended lines, IRAF SPLIT fits and deblends each line separately using predetermined line profiles. Error estimates for blended lines are computed directly in SPLIT by running a number of Monte-Carlo simulations based on preset instrumental parameters.

3.2. Continuum Fitting

The flux-calibrated spectra were corrected for Galactic foreground extinction assuming $E(B - V) = 0.023$ (Schlegel, Finkbeiner, & Davis 1998) and the extinction curve of Cardelli, Clayton & Mathis (1989). After correcting for Galactic extinction, the spectra were converted to F_ν and ν units and the continuum divided in equal size bins, excluding regions containing absorption lines. The statistical 1σ error was determined by estimating the standard deviation within each bin. Next we found that a power law of the form $F_\nu \propto \nu^\beta$ produced an adequate fit to the optical spectrum. The best fitted model changed slightly from $\beta = -0.89 \pm 0.03$ on Feb. 22.66 to $\beta = -1.02 \pm 0.08$ on Feb. 23.66. The continuum points along with the best fitted models are shown in Figure 3. Despite the apparent steepening of the spectra, there is one important caveat, the difficulty of doing spectrophotometry through a narrow slit. Because we have used a 1.5" slit width the throughput of the spectrograph is reduced. Spectrophotometry might also be affected by atmospheric differential refraction (Filippenko 1982). On Feb 22.66 this effect was minimized by aligning the slit at the parallactic angle for the GRB as well as for the spectrophotometric standards. Moreover all the objects were observed at similar airmasses. During Feb 23.66 only one slit angle was used throughout the night and the airmasses for the spectrophotometric standards were slightly higher at the time of acquisition. Therefore, the uncertainty in the spectrophotometry during the second night still allows the possibility that the spectral index did not change between the two nights. The difficulty of achieving accurate spectrophotometry in this case gives more weight to the results obtained from simultaneous multi-band photometry. Our derived spectra index $\beta = -0.89 \pm 0.03$ appears in agreement with the reported single power law $\beta = -0.88 \pm 0.03$ obtained from *BVRI* optical data (Stanek et al. 2001). Moreover the spectral behavior of the lightcurves does not show any steepening of the index β as a function of time (Stanek et al. 2001). The previous result is also consistent with $\beta = -0.89 \pm 0.03$ derived from a low-resolution spectrum obtained five hours after the burst (Jha et al. 2001). But our spectral index is slightly shallower than the index $\beta = -1.1 \pm 0.1$ reported by Masetti et al. (2001). One possible cause for the steepening in the Masetti et al. (2001) results is the inclusion of the *U* band data in the overall fit (Stanek et al. 2001). The bulk of the evidence seems to argue for a single power law spectral index for the duration of the burst. Hereafter we adopt $\beta = -0.89 \pm 0.03$.

Our optical spectral index is similar within uncertainties to the measured X-ray spectral index -0.97 ± 0.05 reported for the whole BeppoSAX observation (in’t Zand et al. 2001). However, as pointed out by these authors, the optical flux is too faint or the X-ray flux is too bright to accommodate a simple synchrotron power-law. One possible explanation for this mismatch is an X-ray excess above the standard synchrotron spectrum due to inverse Compton (IC) scattering (Sari & Esin 2001). Harrison et al. (2001) have recently presented broad-band observations of GRB 000926 that are consistent with this IC interpretation. An alternative explanation for the difference between the optical and X-ray flux is reddening of the optical spectrum. The steep slope of the continuum fit to the optical spectra in addition to the absence of a 2175 \AA “bump” ubiquitous in a Galactic extinction curve implies that the extinction curve intrinsic to GRB 010222 would have to be approximately flat in order to not redden the spectra dramatically. This in turn suggests that the dust content at the burst location is relatively low or that any dust present mimics the gray variety (Aguirre 1999). IR and submillimeter observations of GRB 010222 by Frail et al. (2001b) concluded that the majority of the reprocessed emission seen at the host galaxy is from a separate starburst component. By their estimation thermal radiation or dust scattering near the burst site cannot reproduce the bulk of the observed sub-millimeter energy. Considering the possibility that the host is a starburst galaxy, we estimated the intrinsic reddening using the extinction curve of Calzetti et al. (2000). Dust corrections are particularly dangerous given the complexity of the dust geometry in any particular line of sight (Witt et al. 1992). Nonetheless, even a small color excess, $E(B - V) \approx 0.1$, requires a flatter intrinsic power law for the afterglow with $\beta = -0.39$. This color excess is required to satisfy $\beta = -(p - 1)/2$ for $\nu < \nu_c$ in the optical band and $\beta = -p/2$ at frequencies $\nu > \nu_c$ in the X-ray regime. Here p is the index of the power-law electron energy distribution, and ν_c is the “cooling frequency” at which the electron energy loss time scale is equal to the age of the shock. The spectrum, corrected for such extinction at the host galaxy, is illustrated in Figure 4. Alternatively, it is possible that ν_c has moved below the optical band at the time of our first spectrum, 8.45 hr after the burst. If this is the case, the reddening argument does not apply; instead, an IC scattering interpretation is possible.

4. Analysis

4.1. Metallic Absorption Systems

The statistical properties of metallic absorption systems have been studied extensively at various spectral resolutions (*e.g.*, Steidel & Sargent 1992; Churchill et al. 1999). These studies have provided insight into the equivalent width distribution, evolution, and cosmo-

logical clustering of absorbers. In the particular case of GRB 010222, the equivalent widths of the Mg II doublet in the identified systems indicate that they are unusually strong in comparison to the population of absorbers studied by Steidel & Sargent (1992). The Mg II doublet ratios $W_o(\text{Mg II } 2796.35)/W_o(\text{Mg II } 2803.53)$ are 1.06 ± 0.06 , 1.17 ± 0.19 , and 1.46 ± 0.12 for the $z_1=1.47688$, $z_2=1.15628$ and $z_3=0.92747$ systems, respectively. In each case the ratio differing from 2 implies that the Mg II lines are strongly saturated. In addition to the saturation of Mg II lines, we shall show evidence for saturation effects in the majority of Fe II lines in the ESI spectrum. We avoided using these lines for direct column density measurements given the likelihood of a non-standard curve of growth under saturated conditions (*e.g.*, Morton & Bhavsar 1979).

Instead, resolved absorption lines in the ESI spectrum that are not strongly saturated are more appropriate for column density determinations. The Mn II triplet at 2576.88 Å, 2594.50 Å, and 2606.46 Å in the $z_1=1.47688$ system meets this requirement and appears particularly well suited to studying the highest column absorption system at z_{1b} in which it resides. These lines fall in the region of intermediate optical depth, $\tau \geq 1$, *i.e.*, on the “flat” part of the curve of growth. Here the observed broadening of the Mn II lines is assumed to be due to the random motion of the gas, described by a Maxwellian velocity distribution. In this regime the equivalent width becomes sensitive to the Doppler parameter b , which can be determined directly from the broadening of the absorption lines. The measured Doppler parameters b are listed in Table 3. In order to derive column density N_j for any metal j , we used the general prescription for a standard curve of growth (Spitzer 1978)

$$\frac{W_\lambda}{\lambda} = \frac{2bF(\tau)}{c} \quad (1)$$

$$\tau = \frac{1.497 \times 10^{-2} N_j \lambda f_{ij}}{b} \quad (2)$$

where N_j is written as a function of equivalent width W_λ , rest wavelength λ , oscillator strength f_{ij} , optical depth τ , and its dependence on the Maxwellian velocity distribution $F(\tau)$. Metallic column densities $\log(N_j)$ as well as equivalent neutral hydrogen column densities $\log(N_{\text{HI}})$ assuming solar abundances (Anders & Grevesse 1989) are given in Table 3. Notice the overall agreement in the column densities derived using three different Mn II lines. The column densities listed in the fifth and sixth columns of Table 3 have not been corrected for depletion into dust grains (Jenkins 1987), which is an uncertain quantity.

Waxman & Draine (2000) have shown that dust may be sublimated by a prompt optical/UV flash at any distance closer than ≈ 10 pc from the burst. Fruchter, Krolik & Rhoads

(2001) also considered the possibility of grain charging as a mechanism for dust destruction. This could take place as far away as ≈ 100 pc from the birthsite. Thus, the combined effect of both destruction mechanisms, temperature of the medium, and the return of dust depleted metals to the gas phase make the depletion correction largely uncertain. For completeness we make the simplest assumption ignoring any immediate return of metals into the gas phase and adopt a depletion correction of -1.45 dex for Mn^+ based on Goddard High-Resolution Spectrograph (GHRS) measurements towards ζ Oph obtained by Savage & Sembach (1996). The resulting corrected values are shown in the last column of Table 3. Given the uncertainty in the amount of depletion it appears safe to regard the uncorrected HI column densities as lower limits. We note that the weighted average of Mn^+ corrected for depletion implies $\log(N_{\text{HI}})_{\text{corr}} = 21.89 \pm 0.13 \text{ cm}^{-2}$ in the z_{1a} system, which is similar to the redshift-corrected column density $\log(N_{\text{HI}}) \approx 22.00 \text{ cm}^{-2}$ derived by in 't Zand et al. (2001) from the X-ray afterglow. The results presented so far assume solar abundances, alternatively, less than solar abundances for Mn II might accommodate the difference between metal abundances and the values reported by in 't Zand et al. (2001) and Salamanca et al. (2001).

We have completed the estimates of column densities N_j by including blended absorption lines. The term “blended” is used here to refer to the lines where the z_{1a} and z_{1b} systems cannot be separated cleanly in the ESI spectrum. In particular, by comparing the equivalent widths and the oscillator strength ratios for Zn II (2026.14 Å, 2062.66 Å) and Cr II (2056.25 Å, 2062.23 Å, 2066.16 Å) lines we see that they fall on the linear portion of the curve of growth. For these lines we can obtain a direct measurement of the column density. On the other hand, the Fe^+ and Mg^+ lines, although structured, are strongly saturated. For that reason we decided to fit Gaussian profiles at the positions of the identified z_{1a} and z_{1b} components while running the deblending routines. In this case the linear part of the curve of growth only provides a lower limit to the column density N_j through the equation

$$N_j(\text{cm}^{-2}) = 1.13 \times 10^{17} \frac{W_\lambda(\text{m}\text{\AA})}{f_{ij}\lambda^2(\text{\AA})} \quad (3)$$

The resulting column densities are listed in Tables 3 and 4. In each case the density corresponds to the average of various single transitions. As a consistency check, the HI column density derived assuming solar abundances for the generally undepleted Zn^+ is in agreement with the values cited in Table 3 for the resolved Mn^+ lines.

4.2. Is $z_1=1.47688$ the redshift of GRB 010222?

The absence of any emission lines in the spectrum slightly complicates the unequivocal identification of this system with the host galaxy. However, there is information in the optical spectrum that supports this interpretation. First, the non-detection of a Lyman- α break places an upper limit for the GRB host galaxy of $z \leq 1.96$. Second, Salamanca et al. (2001) have reported evidence of a red wing of Ly- α absorption at $z \approx 1.476$. Third, the measured equivalent widths of the Mg II doublet and the ratio of Mg I to Mg II in this system are also among the highest known for GRB afterglows and for the sample of Mg II absorbers compiled by Steidel & Sargent (1992) at similar spectral resolution. Fourth, we can quantify the probability of detecting three intervening galaxies in the line of sight. The LRIS setup used during the first two nights spans the 3600–9205 Å wavelength range with a rest equivalent width threshold limit $W_o \geq 0.3$ Å, which matches the resolution and equivalent width detection limit of the Steidel & Sargent survey. This wavelength coverage can be translated into a redshift range for Mg II lines of $0.284 \leq z \leq 2.284$, or a redshift interval $\Delta z = 2.0$. Thus, the number of absorbers per unit redshift is $N/\Delta z = 1.5$, which is less stringent than an earlier estimate of this quantity (Jha et al. 2001), but is still larger than the expected number of Mg II absorbers per unit redshift $\langle N/z \rangle = 0.97 \pm 0.10$ for a rest equivalent width threshold of 0.3 Å (Steidel & Sargent 1992). The probability for the chance superposition of three absorbers in this line of sight is non-negligible but small. Lastly, if the highest redshift of an MgII system is $z=1.47688$, then, in 80% of the cases, the source could have originated from no further than $z \approx 1.8$. If it originated from a larger distance then, given the rapid increase in the number of metal absorption systems with increasing redshift, a source redshift higher than $z=1.8$ would be unlikely (Bloom et al. 1997). Although not definitive proof, these arguments are most consistent with the $z_1=1.47688$ absorption system as the host galaxy of GRB 010222.

4.3. Kinematics and abundances of the $z_1=1.47688$ absorption system

The advantage of using higher spectral resolution is the capability to resolve multiple components along the line of sight. In this instance, we identify two kinematic components at $z_{1a}=1.47590$ and $z_{1b}=1.47688$ in the ESI spectrum. The presence of multiple components immediately raises the question of structure within the host galaxy. We might be probing a galactic disk accompanied by an additional kinematic component introduced by absorbing clouds in the halo (Disk-Halo scenario), or instead the two components could be due to absorption arising in distinct regions of a galactic disk (Disk scenario). In order to test these scenarios we also used information about element abundances and dust depletion. In

particular, the ratios $[\text{Zn}/\text{Cr}]$ and $[\text{Zn}/\text{Mn}]$ provide a reasonable measure of the gas-to-dust ratio and the temperature of the absorbing medium.

The main line of argument lending support to a Disk-Halo scenario is the absence of a z_{1a} kinematic component in the resolved set of Mn^+ lines. This is better illustrated in Figure 5, which shows the kinematic components for different metallic lines in velocity space using $z_{1b} = 1.47688$, which is assumed to be the systemic redshift, as the velocity zero point. Mg^0 , Mn^+ and Mg^+ , are present in the z_{1b} system, while the z_{1a} component lacks Mn^+ but contains Mg^+ and some of the structured but likely saturated Fe^+ lines. Since the ionization potential of Mn^+ is almost identical to that of Mg^+ , a possible reason for the absence of Mn^+ at z_{1a} is an underabundance of Mn in a metal-poor environment like the halo. This is based on the conjecture that Type Ia supernovae are an important source of Mn (Samland 1998, Nakamura et al. 1999), or that there is a metallicity dependence yield of Mn in massive stars (Timmes, Woosley, & Weaver 1995), as discussed in the case of damped Ly- α systems by Pettini et al. (2000). An early appearance of type Ia SNe during the halo phase in Milky Way formation models has been questioned (Chiappini, Mateucci, & Romano 2001). If the latter authors are correct, our z_{1a} component might arise in a halo cloud, separated from the velocity zero point by $\approx -119 \text{ km s}^{-1}$, with signatures of Mg^+ and Fe^+ but underabundant in Mn^+ .

The possibility of a Disk-Halo line of sight makes the abundance ratios for each kinematic component that much more crucial in probing the ISM at the host galaxy. Zinc is a fairly reliable metallicity indicator since it resides more than any other metal in the gas phase. On the other hand, metals like Cr and Mn are more easily depleted onto grains and a large fraction of their abundance is contained in metallic dust grains in the galaxy. If the z_{1b} component is an absorption feature of the halo then a higher gas-to-dust ratio than in the disk is expected. Unfortunately, the $[\text{Zn}/\text{Mn}]$ ratio in the z_{1b} component is only an upper limit given that Zn^+ lines from both velocity components are blended, as are the Cr^+ lines. We note however that the Mn and Cr abundances are comparable. In fact the observed $[\text{Zn}/\text{Cr}] \approx 0.61$ is less than $1.61 \geq [\text{Zn}/\text{Cr}] \geq 1.04$ observed towards ζ Oph (Savage & Sembach 1996) and $1.85 \geq [\text{Zn}/\text{Cr}] \geq 0.75$ measured in a sample of 20 sightlines observed with HST (Roth & Blades 1995). Although the $[\text{Zn}/\text{Cr}]$ ratio is less than in any measured Galactic sightline it does not represent a clear discriminant between a halo and a disk or a damped Lyman absorber since the spread in $[\text{Zn}/\text{Cr}]$ is large for either sample (Roth & Blades 1995).

Our results might be an indication of low dust content but not at the extreme reported by Salamanca et al. (2001). It seems that their Zn II measurements are systematically lower than those presented here or any other published results for GRB 010222 (see Jha

et al. 2001, Masetti et al. 2001). In addition, Zn II(2026.14 Å) listed at $\lambda_{obs} = 5011.2$ Å in Table 2 of Salamanca et al. (2001) appears to be a misidentification. We find that line is more consistent with Fe II(2600.17 Å) at the z_3 system while Zn II should be around $\lambda_{obs} = 5018.98$ Å at the higher redshift. For completeness we mention that we have not detected any of the unidentified lines listed in Table 3 of Salamanca et al. (2001) in the region covered by our spectra. Finally, the reduced [Zn/Cr] ratio in the spectrum might be hinting that we have detected a warm medium in the z_{1b} component where depletion for Cr and Mn converge (Savage & Sembach 1996) or else that there is little dust to deplete onto in this environment. A warmer medium would result in different dust depletion corrections and lower the inferred values of N_{HI} assuming standard solar abundances. These results are in agreement with the depletion patterns discussed by Savaglio et al. 2002.

We now consider the alternative of a Disk scenario. In general, any neutral Mg present in a galactic disk must be shielded from external photoionizing flux. A feasible scenario is that we are probing a line of sight passing through two distinct regions within the disk containing neutral gas. These regions could be underdepleted molecular clouds cocooning Mg in its neutral form. A possible consequence of uneven photoionization in the disk is the marginal detection of a blue “wing” on the z_{1a} component of the Mg II (2796.35 Å) absorption line (Figure 5). This feature would argue for a stronger photoionizing source near the closer side of the disk and against a galactic halo. This option would eliminate the necessity for a halo component, but it does not explain the absence of Mn^+ in the z_{1a} system, assuming similar enrichment processes for different parts of the disk. Instead, there may be a strong metallicity gradient along the disk, as has been observed along the disk of the Milky Way (van Steenberg & Shull 1988). Assuming that a Disk scenario is correct and that the [Zn/Mn] ratio peaks towards the inner part of the host galaxy; the velocity systems might be tracing a fraction of galactic rotation. Independent of the interpretation, the presence of a galactic disk appears necessary to explain the properties of the strongest absorption system. This furthers the connection of long-duration GRBs with a disk progenitor.

4.4. Looking for signatures of H_2 absorption and Fluorescence

The impact of the associated UV flash on H_2 molecules in the vicinity of a GRB has been determined by Draine (2000). The direct observable consequence of strong UV radiation from a GRB on the surrounding H_2 is the production of vibrationally excited levels which could create strong line absorption in the region $912 \text{ Å} \leq \lambda_{rest} \leq 1650 \text{ Å}$, and reradiated fluorescent emission in a similar range. For a redshift of $z = 1.477$ this corresponds to the region $\lambda_{obs} \leq 4087 \text{ Å}$. Unfortunately the region where the absorption effect is strongest at

$\lambda_{\text{obs}} \approx 3096 \text{ \AA}$ falls outside our spectral coverage. Thus, we are only able to probe a fraction of the absorption region near the blue end of the spectrum where the quantum efficiency is low and the noise is high. The strength of the absorption depends on the amount of H_2 available for vibrational excitation. At the LRIS resolution we find no definite evidence of H_2 absorption for $\lambda_{\text{obs}} \leq 4087 \text{ \AA}$ to make a proper determination of N_{H_2} . However, our spectra probably rule out excited states of H_2 at $N_{H_2} \geq 10^{20} \text{ cm}^{-2}$ based on the transmission plots of Draine (2000).

4.5. Absorption-line variability

If the line absorption occurs sufficiently close to the burst site, the afterglow emission could manifest itself through photoionization of the GRB environment, thus, variability of the absorption features. To detect this time-dependent effect various snapshots of the absorption spectrum are required. In this particular instance we take advantage of the low-resolution spectra obtained over two consecutive nights to search for the predicted effect. The measured equivalent widths for each night as well as the statistical uncertainties are listed in Table 1. Comparison between the LRIS equivalent widths on consecutive nights shows no strong evidence for time dependence of the absorption lines within statistical uncertainties. There is also an overall agreement with the ESI measurements. We deduce that discrepancies in any two measurements are mainly due to uncertainties in the continuum level in the vicinity of each line. There does seem to be a systematic trend of larger equivalent widths on the second night below 5403.80 \AA . However, we also note that it is clear from the spectrum that the equivalent widths of lines on the blue side are relatively “weak” with respect to well detected lines on the red side where such trend is not detected. Hence, at this point we cannot attribute the systematic trend entirely to a physical effect since the relative line flux measurements might have been affected by the continuum fitting during the second night as discussed in §3.1 and §3.2.

Although the equivalent width depends on the overall characteristics of the continuum, its main uncertainty is defined locally by the error in determining the proper level of the continuum on either side of the line of interest. As discussed in §3.1 the errors quoted for equivalent widths correspond to a Poisson model of the noise in the region of interest. Such an assumption might be oversimplified and not account for true variations in the continuum, but we believe that we safeguard against strong systematic effects by using the same, consistent method in all measurements. Hence based on our analysis we do not find statistically significant changes in our measurements. Taking this comparison further there are published equivalent width measurements for this burst elsewhere (Jha et al. 2001, Masetti et al

2001, Salamanca et al. 2001). Although the duration of observation, spectral resolution and brightness of the burst varies in each case, the reported measurement techniques are similar. Direct comparison finds that our results are consistent with previous measurements. Nevertheless some differences are present in a few cases such as C IV, Cr II and Zn II that were discussed in §4.3. However, we do not find systematic and statistically significant changes as a function of time in the published data that should be present if either photoionization or dust destruction in the circumburst medium are actively dominant for similar species. We refrain from reporting a measurement for Al III(1862.79 Å) during the second LRIS spectrum in Table 1 because of the reduced signal-to-noise in that region of the spectrum. For completeness we note that the line has not disappeared and it is clearly detected in the ESI spectrum obtained at a comparable time (Table 2).

5. Photoionization Code

In order to interpret our observations under constraints imposed by the lack of absorption-line variability, we simulated the GRB environment using a standard photoionization model. The photoionization evolution has been described by Perna & Loeb (1998) and Böttcher et al. (1999). The photoionization rate can be written in the following form:

$$-\frac{1}{n_j(r, t')} \frac{dn_j(r, t')}{dt'} = \int_{\nu_{0,j}}^{\infty} d\nu' \frac{F_{\nu'}(r, t')}{h\nu'} \sigma_{\text{bf},j}(\nu'), \quad (4)$$

where n_j is the density for species j , $F_{\nu'}(r, t')$ is the flux at radius r , t' is the elapsed time in the GRB frame and $\sigma_{\text{bf},j}(\nu')$ is the photoionization cross section at frequency ν' using the analytical fits provided by Verner et al. (1996). We neglect recombination processes since the densities we will be considering are typically $n \leq 10^6 \text{ cm}^{-3}$, where the corresponding recombination timescales are much longer than the duration of the GRB and our observations (Perna & Loeb 1998). In addition the full effect of dust destruction and the return of depleted metals into the gas phase has been ignored in the code.

Next we constructed the input flux $F_{\nu'}(r, t')$ for this particular afterglow from the observed time decay (Stanek et al. 2001) and the measured optical spectral index. The function has two forms to accommodate the observed break in the light-curve at $t_{\text{break}}=0.72$ day. Thus

for $t \leq 0.72$ day

$$F_{\nu}(r_0, t') = 5.26 \times 10^{-28} \left(\frac{\nu'}{6.94 \times 10^{14}(1+z)\text{Hz}} \right)^{-0.89} \left(\frac{d^2}{(1+z)r_0^2} \right) \left(\frac{t'(1+z)}{0.352 \text{ day}} \right)^{-0.80} \text{ ergs cm}^{-2} \text{ sec}^{-1} \text{ Hz}^{-1} \quad (5)$$

otherwise

$$F_{\nu}(r_0, t') = 2.97 \times 10^{-28} \left(\frac{\nu'}{6.94 \times 10^{14}(1+z)\text{Hz}} \right)^{-0.89} \left(\frac{d^2}{(1+z)r_0^2} \right) \left(\frac{t'(1+z)}{0.72 \text{ day}} \right)^{-1.30} \text{ ergs cm}^{-2} \text{ sec}^{-1} \text{ Hz}^{-1} \quad (6)$$

where d is the luminosity distance to the burst at $z = 1.47688$ (assuming $H_0 = 65 \text{ km s}^{-1} \text{ Mpc}^{-1}$, $\Omega_m = 0.3$, $\Lambda = 0.7$), and $r_o = 10^{17} \text{ cm}$ is the inner radius of the photoionized region set as a boundary condition. We have used the observed flux and ignored any intrinsic dust corrections. In a previous section we showed that intrinsic reddening following a Calzetti et al. (2000) extinction law for starbursts would dim and steepen an intrinsically flat spectrum. The effect of using an input flux uncorrected for intrinsic extinction is to slow down the time-dependence in our models; therefore, the integration times presented here should be considered upper limits. The input flux has been integrated in the UV range up to a cutoff energy of 0.2 keV. The reasoning behind this choice is partly arbitrary given the failure to locate a precise spectral break at the “cooling frequency” ν_c between the optical and X-ray ranges. The selected cutoff energy of 0.2 keV represents roughly the region where the photoionization cross section for the species of interest has dropped sharply. Above 0.5 keV, X-rays are mostly absorbed by heavy elements.

We start the photoionization of a pristine neutral medium at initial time t'_o that follows the detection of prompt emission in the BeppoSAX energy band. The transition between the prompt GRB emission and the onset of the afterglow is not a very well defined point observationally. Variability arguments set the scale for internal shocks to take place in a region of size $R \approx 3 \times 10^{14} \text{ cm} (\delta t/1 \text{ s})(\Gamma/100)^2$. External shocks responsible for the afterglow become significant at $\approx 10^{16} \text{ cm}$ from the source (Piran 1999). For numerical reasons we have selected an initial time of $t'_o = 10$ seconds for the onset of photoionization.

The photoionization process can be pictured as occurring inside a sphere of outer radius r_{max} , subdivided into thin spherical shells of width Δr so that each shell i is optically thin. In each shell the initial incident flux spectrum described above will be absorbed and will also follow a r^{-2} law as $r \rightarrow r_{\text{max}}$. Hence the incident spectrum at any shell i will be given by:

$$F_{\nu'}(r_{i+1}, t') = F_{\nu'}(r_i, t') e^{-\tau_{\nu,i}} \left(\frac{r_i}{r_{i+1}} \right)^2 \quad (7)$$

We ignore bound-bound processes therefore $\tau_{\nu,i}$ stands for the photoionization optical depth which is estimated within each shell i as:

$$\tau_{\nu,i} = \Delta r \sum_a n_j(r, t') \times [\sigma_{\text{bf},a}(\nu')] \quad (8)$$

where $\tau_{\nu,i} \ll 1$. For our models we included H, He, and Mg and neglected other elements. The initial number density n_j for each species is largely unknown but we decided to use standard solar-system abundances. For simplicity we also assumed that initially Mg is equally divided into Mg^0 and Mg^{+1} .

6. Numerical Results *vs.* Physical Conditions

Since the depletion correction/abundance and therefore the total N_{H} near the burst site is not well determined, we examined the time dependence of equivalent widths for two different hydrogen column densities. The first, $\log(N_{\text{HI}}) = 20.44 \text{ cm}^{-2}$ represents the inferred HI column ignoring any dust depletion correction and takes into account the possibility of complete circumburst dust destruction. The second, $\log(N_{\text{HI}}) = 22.00 \text{ cm}^{-2}$ is appropriate for standard Milky Way depletion onto dust or perhaps less than solar metal abundances. The latter is also consistent with measurements of the red wing of a possible Ly α feature (Salamanca et al. 2001), and the BeppoSAX afterglow results (in't Zand et al. 2001). In each case we chose four different combinations of number densities n_{HI} and r_{max} to reproduce the simulated hydrogen column density $N_{\text{HI}} = n_{\text{HI}} \times r_{\text{max}}$. The parameters for each model are listed in Table 5. The denser, more compact models represent the conditions in dense molecular clouds which have been postulated as a potential ambient environment for the progenitors of GRBs. On the other hand, the low density and extended environments are compatible with low density molecular clouds, young stellar clusters, and possibly galactic superbubbles (Scalo & Wheeler 2001).

We considered it relevant to trace the time evolution of two particular absorption lines present in our spectra, Mg I (2852.96 Å) and Mg II (2796.35 Å). Mg I is an appealing line given the possibility of encountering Mg in its neutral form in regions of the galaxy shielded from photoionization. Mg II(2796.35 Å) is of interest because of its detection in a number of GRB spectra. An additional observational reason for choosing these particular lines to test

our models is the consistency of the line flux measurements on the red side of the spectrum where the effects of differential refraction appear of less importance. In order to model our observations, we integrated to a maximum time $t_{\text{max}} = 32.45$ hours after the GRB, when the second LRIS spectrum was obtained. The equivalent width at different stages was estimated using equations (1) and (2) which return W_λ . Throughout our calculations we have assumed a constant Doppler parameter b representative of the system (see Table 3). This appears to be a fairly robust assumption since the time dependence for the lines is mainly a function of the photoionization equations.

Figure 6 illustrates the time evolution of the equivalent width for Mg I (2852.96 Å) and Mg II (2796.35 Å) in a $\log(N_{\text{HI}}) = 20.44 \text{ cm}^{-2}$ environment. The times when the LRIS spectra were obtained are indicated. Notice the distinct differences in the line evolution in each case. The denser, more compact models are ionized rather rapidly since most of the gas is close to the GRB and gets impacted by a large flux. On the other hand, less dense models representative of thin galactic environments require longer for noticeable effects to take place. The $n_{\text{HI}} = 89 \text{ cm}^{-3}$, $r_{\text{max}} = 1 \text{ pc}$ model appears to mark the line where our low-resolution spectroscopy would have been able to detect time dependence with this column density. Denser environments than this appear to be disfavored according to our model.

Figure 7 shows the time dependence for a $\log(N_{\text{HI}}) = 22.00 \text{ cm}^{-2}$ environment. Similarly compact, high density environments are photoionized rather quickly while extended, less dense ones would evolve with a shallower decline. The $n_{\text{HI}} = 2 \times 10^4 \text{ cm}^{-3}$, $r_{\text{max}} = 5.0 \times 10^{17} \text{ cm}$ model is close to our detection limit for this denser environment. The results in this case are more dependent on the choice of the inner radius r_o because the scale of some of the models becomes comparable to r_o . A different choice for the inner radius would either accelerate or delay the photoionization timescale, therefore, compact models with this column density are more tentative. However, it appears that very dense, compact environments would have been more highly ionized than is observed in our initial spectrum.

One interpretation of X-ray and optical afterglow data from GRB 010222 invokes a transition from a relativistic to a non-relativistic regime, and consequently the deceleration of the shock, to account for the break in the light curve (in 't Zand et al. 2001). This scenario requires an environment with $n_{\text{HI}} \approx 10^6 \text{ cm}^{-3}$ and size $\approx 10^{16} \text{ cm}$. Although our simulations argue against the presence of a dense 10^{16} cm neutral gas slab between the two observations, we cannot rule out the presence of a large density slab at the time of the burst itself. However our modelling also presents an alternative scenario for more extended N_H absorption in the host galaxy rather than a single slab. Recent modelling of the multiwavelength observations of GRB 010222, including the radio emission, finds that a jet model expanding into homogeneous external medium with density $n_{\text{HI}} \approx 3.2 \text{ cm}^{-3}$

is consistent with the broadband data (Panaitescu & Kumar 2001). A jet and low-density interpretation is also required to satisfy the standard-energy output with beaming corrections of Frail et al. (2001a). One final point in this discussion is the shape of the γ -ray burst light curve and baryon contamination. A very dense nearby medium gives rise to high optical depth τ where baryons could prevent relativistic expansion. The overall effect could lead to “dirty” fireballs and smearing of the γ -ray profile. Instead the burst profile appears highly structured (in ’t Zand et al. 2001).

Consider now the actual column density to this burst if the host galaxy has a dust-to-gas ratio similar to that of the Milky Way. A color excess of $E(B - V) = 2.00$ mag is estimated for $\log(N_{\text{HI}}) = 22.00$ cm^{-2} and assuming a Galactic conversion $N_{\text{HI}}/E(B - V) = 5.0 \times 10^{21}$ cm^{-2} mag^{-1} (Savage & Mathis 1979). This is significantly larger than $E(B - V) = 0.06$ mag for a $\log(N_{\text{HI}}) = 20.44$ cm^{-2} environment. It is possible that the UV emission from the burst is responsible for destruction of neighboring dust in the high-density case (Galama & Wijers 2001), but further extinction at larger distances is expected along the line of sight unless the burst is near the Earth-facing side of the host galaxy (Reichart & Price 2002). We must keep in mind, however, the possibility that we are probing different scales in two separate energy bands.

7. Implications for the Nature of the GRB 010222 Progenitor Environment

GRB 010222 is a good candidate to explore whether we can place constraints on the progenitor environment. The kinematic components resolved in the high-resolution spectrum give support to a location of this burst in a galactic disk. High-resolution spectroscopy of GRB 000926 (Castro et al. 2001b) favors a similar interpretation for that burst. The slope of the spectral continuum in this instance suggests that the burst occurred in a dust-free environment or was surrounded by a screen of gray dust (Aguirre 1999). Near-IR and submillimeter observations by Frail et al. (2001b) also appear to rule out the possibility of strong dust scattering or thermal emission near the GRB site. However it is difficult to model *a priori* the properties of dust at this redshift since the distribution and properties of galactic dust as a function of redshift are largely unknown.

7.1. Isolated Molecular Clouds

Popular models of gamma-ray burst progenitors include young massive stars (Woosley 1993, Vietri & Stella, 1998). This makes the interior of molecular clouds a potential birth-

place for GRBs. Molecular clouds tend to comprise large amounts of dust and clumpy pockets of gas ideal for star formation. If GRB 010222 took place in a molecular cloud, the slope of the optical continuum indicates that either the nearby dust was destroyed rather immediately by the burst through a combination of sublimation by an optical/UV flash (Waxman & Draine 2000) and grain charging (Fruchter, Krolik & Rhoads 2001) or that the surrounding dust content was low prior to the explosion. The absence of measurable signatures of metals being returned to their gas phase as a by-product of dust destruction on such a short timescale does not allow direct distinction between these two possibilities. However, a high fraction of dust results in a larger H_2 formation rate since molecular hydrogen tends to form in reactions taking place on grains. The absence of strong absorption features due to vibrational excited levels of H_2 expected from strong UV emission impacting the surrounding H_2 that might permeate a progenitor in a dusty molecular cloud (Draine 2000) is conspicuous. Moreover, assuming a mean density of 10^4 cm^{-3} and the typical size of a dense molecular cloud, the absorption lines detected should have weakened over the period of our observations. A massive and dense molecular cloud might also give rise to reflection at 6.4 keV as seen near the Galactic center (Murakami, Koyama, & Maeda 2001). Nevertheless, it is still viable that a molecular hydrogen detection has been made blueward of our spectral limit by Lee et al. (2001) and Galama et al. (2002). As reported by these authors the flux deficit in the U band which extends below 3500 \AA does not fit the SMC or LMC-like extinction models. A depression signature is also expected if there is absorption by a Lyman- α wing (Salamanca et al. 2001). The absence of molecular hydrogen and reduced depletion resulting from the $[\text{Zn}/\text{Mn}]$ and $[\text{Zn}/\text{Cr}]$ ratios still allows the location of the GRB to be near the edge of a molecular cloud prior to the explosion. Thus, at the time of the event the fraction of gas to dust can be larger than at the center of the cloud, inhibiting the formation of H_2 . Immediately after the onset of the UV emission from the burst, any remaining dust could have been destroyed efficiently by the expanding UV radiation pulse, minimizing reddening of the optical continuum.

7.2. Superbubbles

Panaiteescu & Kumar (2001) in their multiwavelength analysis of well-studied afterglows found that the ambient density for some bursts can be as low as $1.9 \times 10^{-3} \text{ cm}^{-3}$; however, some arguments favor higher ambient densities once the complete radio data set is included in the analysis of individual bursts (Berger et al. 2002). The presence of low densities led Scalo & Wheeler (2001) to argue for active star formation regions in superbubbles as possible environments for GRBs. Our photoionization models show that low-density environments with the typical sizes of superbubbles would not produce strong time-dependence in absorp-

tion lines. Moreover, the interior of a superbubble could be partially ionized prior to the GRB event. The prior ionization might be accomplished via overlapping ionization bubbles generated by supernovae in clusters of massive stars. A pre-ionized environment decreases the amount of neutral material seen by the expanding photoionization front and prevents the full effect of time-dependent absorption. But it also enables the detection of time dependence in high-ionization species. We detect high-ionization C IV absorption in our low-resolution spectrum, but it is not clear that equivalent width variations are seen. In general C IV is a tracer of additional diffuse warm and hot gas that could originate in a superbubble environment. Unfortunately, our high-resolution spectrum does not cover this absorption line to firmly establish if it comes from the disk of the host galaxy or rather from a gaseous halo. We note however that the equivalent width of C IV (1548.20 Å) is comparable to that of the Mg II absorption lines. An additional signature of prior ionization could be the attenuation of the X-ray continuum by an ionized absorber like those seen in AGN spectra. The absence of strong absorption features except for a marginal Fe XIV-XVIII edge suggested by in 't Zand et al. (2001) prevents a straightforward connection from being made between X-ray and UV absorption features.

An advantage of the superbubble scenario is the availability of a dust destruction mechanism and a favorable geometry for observation. The combination of winds and SN explosions would tend to blow the gas and dust away leaving filamentary or shell-like patterns like the one reported in the Galactic Orion-Eridanus bubble (Guo et al. 1995). In addition, winds and radiation pressure in the interior of a superbubble might selectively destroy small grains, a mechanism for gray dust production locally. However, this selective process is balanced by rapid destruction of large grains by the burst and earlier destruction by X-rays emitted inside the superbubble that might lead to grain charging (Fruchter, Krolik, & Rhoads 2001). In combination, these two processes could counteract the expulsion of small grains and suppress the formation of gray dust. Either dust destruction or its gray nature are consistent with the slope of the observed continuum and the lack of strong dust reprocessing near the burst site (Frail et al. 2001b). The only practical problem with this interpretation is the mismatch between the optical and X-ray spectra. It is possible that the cooling frequency has moved out of the optical band. In this case we propose that the observed X-ray excess (in 't Zand et al. 2001) is mostly due to inverse Compton scattering rather than intrinsic reddening near the burst location but if true the ambient density cannot be below a few cm^{-3} or inverse Compton scattering would be suppressed (Harrison et al. 2001). If the effects of dust depletion are less pronounced than in the Milky Way, a $\log(N_{\text{HI}}) = 20.44$ cm^{-2} environment with $n_{\text{HI}} \leq 89$ cm^{-3} and $r_{\text{max}} \geq 1$ pc is suggested for GRB 010222. This is consistent with the best-fitted parameter $n_{\text{HI}} \approx 3.2$ cm^{-3} resulting from jet modelling (Panaitescu & Kumar 2001).

7.3. Young Stellar Clusters

The recently discovered Arches cluster (Nagata et al. 1995; Cotera et al. 1996; Serabyn, Shupe, & Figer 1998; Figer et al. 1999) consists of more than 100 young stars with masses greater than $20 M_{\odot}$ within a $\approx 0.3 - 0.4$ pc radius. Radio observations of the Arches stellar cluster have confirmed the presence of powerful ionized winds with mass-loss rates $\approx (1 - 20) \times 10^{-5} M_{\odot} \text{ yr}^{-1}$ coincident with massive stars in the cluster (Lang, Goss, & Rodriguez 2001). If a low metallicity massive star that has lost its envelope turns out to be the prototype for the collapsar model of GRBs (MacFadyen & Woosley 1999), a young stellar cluster environment appears to be a perfect cradle for progenitors as prelude to GRB formation. A compact young cluster environment is consistent with our observations and models but requires low dust content or rapid destruction near the burst site, as well as photoionization of the gas in the region by hot young stars prior to the GRB. The complexity of wind interaction and shocks might provide favorable dust viewing geometries and dust distribution similar to those discussed in the superbubble scenario. In addition, the UV absorption lines and their lack of time dependence might be attributed to the medium well outside the stellar cluster where the photoionizing flux is not strong enough to imprint substantial changes. One problem with this interpretation is the type of metallicities required by the MacFadyen & Woosley (1999) model which can be thought of as LMC-like (A.I. MacFadyen 2002, private communication). The abundances in the GRB 010222 host are larger than the abundances reported in LMC line of sights (Welty et al. 1999). In addition, the absence of strong signatures of ionized absorption and pronounced emission lines in the X-ray spectrum (in't Zand et al. 2001) might argue against a pre-ionized medium.

7.4. Halo

An alternative GRB progenitor is a coalescing compact object (Neutron Star-Neutron Star, Black Hole-Neutron Star) (Paczynski 1986). Even though the distribution of birth kick velocities for compact objects has not been fully surveyed, typical velocities around a few hundred km s^{-1} could place a fraction of potential progenitors at high-latitude above the disk. The apparent presence of a galactic disk in this case seems to rule out the possibility of a halo origin for GRB 010222. Even though a location in the halo implies a low-density environment, the ionized regions of interest would be relatively compact clouds in the halo. In this case, it is difficult to reproduce the measured neutral column densities and observed time evolution in a halo event. Photoionization in halo events might be more effective in erasing absorption features entirely if the line-of-sight does not intercept the disk of the host galaxy. Current ideas suggest that the hard-short class of GRBs are due to coalescing

compact objects (Janka *et al.* 1999, Fryer *et al.* 1999). Rapid localization of the hard-short GRBs might allow the detection of absorption-line time dependence in high-ionization species following coalescence in a galactic halo.

8. Conclusions and other Observational Reflections

The use of high-resolution spectroscopy has resolved the host galaxy of GRB 010222 into multiple components. We conclude that the GRB took place in a galactic disk that gives rise to the strongest absorption system. The power-law index of the optical continuum indicates that the dust content at the burst place is low or that the reddening follows a gray dust model. Under these conditions the bulk of the X-ray excess (in 't Zand *et al.* 2001) can be attributed to inverse Compton scattering. Low resolution spectroscopy obtained over the span of two days failed to reveal any significant evidence for time dependence of the observed absorption lines. Signatures of strong H_2 absorption and/or fluorescence are also absent from our spectra. Photoionization models constructed to test a range of initial conditions for this burst show that dense, compact media would be photoionized fairly quickly while less dense media with large radii evolve slower with time. We argue that prior to a GRB, an environment partially ionized either by the progenitor or by nearby sources would prevent the full manifestation of predicted absorption-line evolution. The physical attributes of GRB 010222 are consistent with a low-density molecular cloud, superbubble, or young stellar cluster as the possible environment of the GRB.

In the future some consideration should be given to a prompt optical-UV flash like the one accompanying GRB 990123. The intensity of such an event could in principle lead to dust destruction, but it might also be responsible for the photoionization of a fraction of the neutral gas. The full effect of such a flash has been ignored in our models. Preferentially, the observation of time-dependent absorption lines would work best in bursts occurring in the Earth-facing side of the host galaxy and in compact regions. Our analysis suggests that this technique applied with high-resolution spectroscopy could potentially distinguish the metallicity of progenitor environments. In that regard shortening the interval between burst localization and initial spectroscopy becomes crucial to exploring earlier, less photoionized times. The next generation of high-resolution imagers might directly resolve the environment of GRBs in a relatively nearby host galaxy. A prospect raised by the observations of GRB 010222 is the study of the properties of galactic dust at high-redshift using bursts as beacons to illuminate the dust nearby. Further exploration of this issue is encouraged as spectroscopy is obtained for a larger sample of GRBs.

We would like to thank R. -P. Kudritzki and F. Bresolin for obtaining the first set of spectra as well as H. Spinrad, D. Stern, A. Dey, A. Bunker, and S. Dawson for taking the second set of LRIS spectra. We also acknowledge Eric Gotthelf for allowing us to use his new Alpha computer and Robert Uglesich for tips on optimization in FORTRAN. This work was supported by the National Science Foundation under Grant No. AST-00-71108. JSB is supported as a Fannie and John Hertz Fellow.

REFERENCES

- Aguirre, A. 1999, *ApJ*, 525, 583
- Aguirre, A. & Haiman, Z. 1999, *ApJ*, 532, 28
- Anders, E., & Grevesse, N. 1989 *Geochim. Cosmochim. Acta* 53, 197
- Berger, E., Sari, R., Frail, D., & Kulkarni, S. 2001, in *Gamma-Ray Bursts in the Afterglow Era* (Berlin: Springer), 218
- Bloom, J. S., Sigurdsson, S., Wijers, R. A. M. J., Almaini, O., Tanvir, N. R., & Johnson, R. A. 1997, *MNRAS*, 292, 55
- Bloom, J. S., Djorgovski, S. G., Kulkarni, S. R., & Frail, D. A. 1998, *ApJ*, 507, L25
- Bloom, J. S., Kulkarni, S. R., & Djorgovski, S. G. 2002, *AJ*, 123, 1111
- Bloom, J. S., Djorgovski, S. G., Halpern, J. P., Kulkarni, S. R., Galama, T. J., Price, P. A., Castro, S. M. 2001, *GCN Circular* 989
- Böttcher, M., Dermer, C. D., Crider, A. W., & Liang, E. P. 1999, *A&A*, 343, 111
- Calzetti, D., Armus, L., Bohlin, R. C., Kinney, A. L., Koornneef, J., & Storchi-Bergmann, T. 2000, *ApJ*, 533, 682
- Cardelli, J. A., Clayton, G. C., & Mathis, J. S. 1989, *ApJ*, 345, 245
- Castro, S. et al. 2001a, *GCN Circular* 999
- Castro, S., Galama, T. J., Harrison, F. A., Holtzman, J. A., Bloom, J. S., Djorgovski, S. G., & Kulkarni, S. R. 2001b, *astro-ph/0110566*
- Chiappini, C., Matteucci, F. & Romano, D. 2001, *ApJ*, 554, 1044
- Churchill, C. W., Rigby, J. R., Charlton, J. C., & Vogt, S. S. 1999, *ApJS*, 120, 51
- Cotera, A. S., Erickson, E. F., Colgan, S. W. J., Simpson, J. P., Allen, D. A., & Burton, M. G. 1996, *ApJ*, 461, 750
- Djorgovski, S. G., Kulkarni, S. R., Bloom, J. S., Goodrich, R., Frail, D. A., Piro, L., & Palazzi, E. 1998, *ApJ*, 508, 17
- Draine, B. T. 2000, *ApJ*, 532, 273
- Figer, D. F., Sungsoo, S. K., Morris, M., Serabyn, E., Rich, R. M., & McLean, I. S. 1999, *ApJ*, 525, 750
- Filippenko, A. 1982, *PASP*, 94, 715
- Frail, D. A. et al. 2001a, *ApJ*, 562, L55
- Frail, D. A. et al. 2001b, *astro-ph/0108436*

- Fruchter, A. S., Krolik, J. H., & Rhoads, J. E. 2001, *ApJ*, 563, 597
- Fryer, C. L., Woosley, S. E., Herant, M., & Davies, M. B. 1999, *ApJ*, 520, 650
- Galama, T. J., & Wijers, R. A. M.J. 2001, *ApJ*, 549, 209
- Galama, T. J. et al 2002, in preparation
- Guo, Z., Burrows, D. N., Sanders, W. T., Snowden, S. L., & Penprase, B. E. 1995, *ApJ*, 453, 256
- Harrison, F. A., et al. 2001, *ApJ*, 559, 123
- Henden, A. 2001a, GCN Circular 961
- Henden, A. 2001b, GCN Circular 962
- in 't Zand, J. J. M. et al. 2001, *ApJ*, 559, 710
- Janka, H.-T., Eberl, T., Ruffert, M. & Fryer, C. L. 1999, *ApJ*, 527, L39
- Jenkins, E. B. 1987, in *Interstellar Processes* (Dordrecht: Reidel), 533
- Jha, S., et al. 2001, *ApJ*, 554, L155
- Klebesadel, R. W., Strong, I. B., & Olson, R. A. 1973, *ApJ*, 182, 85
- Lang, C. C., Goss, W. M., & Rodriguez, L. F. 2001, *ApJ*, 551, L143
- Lee, B. C., et al. 2001, *ApJ*, 561, L183
- MacFadyen, A. I. & Woosley, S. E. 1999, *ApJ*, 524, 262
- Masetti, N., et al. 2001, *A&A*, 374, 382
- Mészáros, P., & Rees, M.J. 1997, *ApJ*, 476, 232
- Morton, D. C., & Bhavsar, S. P. 1979, *ApJ*, 228, 147
- Morton, D. C. 1991, *ApJS*, 77, 119
- Murakami, H., Koyama, K. & Maeda, Y. 2001, *ApJ*, 558, 687
- Nakamura, T., Umeda, H., Nomoto, K., Thielemann, F., & Burrows, A., et al. 1999, *ApJ*, 517, 193
- Nagata, T., Woodward, C. E., Shure, M., & Kobayashi, N. 1995, *AJ*, 109, 1676
- Panaitescu, A., & Kumar, P. 2001, *ApJ*, 560, L49
- Paczyński, B. 1986, *ApJ*, 308, L43
- Perna, R., & Loeb, A. 1998, *ApJ*, 501, 467
- Pettini, M., Ellison, S. L., Steidel, C. C., Shapley, A. E., & Bowen, D. V. 2000, *ApJ*, 532, 65
- Piran, T., 1999, *Phys. Rep.*, 314, 575

- Piro, L., et al. 2000, *Science*, 290, 955
- Piro, L., 2001, *GCN Circular* 959
- Reichart, D. E. & Price, P. A. 2002, *ApJ*, 565, 174
- Roth, K. C., & Blades, J. C. 1995, *ApJ*, L95
- Salamanca, I., et al. 2001, *astro-ph/0112066*
- Samland, M. 1998, *ApJ*, 496, 155
- Sari, R., & Piran, T. 1997, *ApJ*, 485, 270
- Sari, R., & Esin, A. A. 2001, *ApJ*, 548, 787
- Savage, B. D., & Mathis, J. S. 1979, *ARA&A*, 17, 73
- Savage, B. D., & Sembach, K. R. 1996, *ARA&A*, 34, 279
- Savaglio, S., Fall, S. M., & Fiore, F. 2002, *astro-ph/0203154*
- Scalo, J. & Wheeler, J. C. 2001, *ApJ*, 562, 664
- Schlegel, D. J., Finkbeiner, D. P., & Davis, M. 1998, *ApJ*, 500, 525
- Serabyn, E., Shupe, D., & Figer, D. F. 1998, *Nature*, 394, 448
- Spitzer, L. 1978, in *Physical Processes in the Interstellar Medium* (New York: Wiley), 51
- Stanek, K. Z., et al. 2001, *ApJ*, 563, 592
- Steidel, C. C., & Sargent, W. L. W. 1992, *ApJS*, 80, 1
- Timmes, F. X., Woosley, S. E., & Weaver, T. A. 1995, *ApJS*, 98, 617
- van Steenberg, M. E., & Shull, J. M. 1988, *ApJ*, 330, 942
- Verner, D. A., Barthel, P. D., Tytler, D. 1994, *A & A*, 108, 287
- Verner, D. A., Ferland, G. J., Korista, K.T., & Yakovlev, D.G. 1996, *ApJ*, 465, 487
- Vietri, M. & Stella, L. 1999, *ApJ*, 527, L43
- Vreeswijk, P. M. et al. 2001, *ApJ*, 546, 672
- Waxman, E., & Draine, B.T. 2000, *ApJ*, 537, 796
- Welty, D. E., Frisch, P. C., Sonneborn, G. & York, D. G. 1999, *ApJ*, 512, 636
- Witt, A. N., Thronson, H. A., & Capuano, J. M. 1992, *ApJ*, 393, 611
- Woosley, S. E. 1993, *ApJ*, 405, 273

Table 1. LRIS Line Identification

Line($\lambda_{\text{vac}}(\text{\AA})$)	$\lambda_{\text{helio}}(\text{\AA})$	z	f_{ij}	$W_1(\text{\AA})^c$	$W_2(\text{\AA})^d$
Si II(1526.71 \AA)	3782.12	1.4773	1.10×10^{-1}	1.51 ± 0.13	1.72 ± 0.47
C IV(1548.20 \AA)	3835.36	1.4773	1.91×10^{-1}	2.55 ± 0.23	2.67 ± 0.29
+ C IV(1550.78 \AA) ^b			9.52×10^{-2}		
Fe II(1608.45 \AA)	3984.61	1.4773	6.19×10^{-2}	0.40 ± 0.04	0.52 ± 0.30
Al II(1670.79 \AA)	4138.77	1.4771	1.83	1.48 ± 0.09	1.58 ± 0.12
Si II(1808.01 \AA)	4478.51	1.4770	5.53×10^{-3}	0.60 ± 0.08	0.81 ± 0.15
Al III(1854.72 \AA)	4592.77	1.4763	5.60×10^{-1}	0.79 ± 0.06	0.94 ± 0.13
Fe II(2382.77 \AA) ^a	4592.77	0.9275	3.01×10^{-1}	1.01 ± 0.08	1.21 ± 0.17
Al III(1862.79 \AA)	4614.50	1.4772	2.79×10^{-1}	0.69 ± 0.08	. . .
Zn II(2026.14 \AA)	5018.95	1.4771	4.89×10^{-1}	0.71 ± 0.07	1.03 ± 0.13
+Mg I(2026.48 \AA) ^b			1.15×10^{-1}		
Cr II(2056.25 \AA)	5093.54	1.4771	1.05×10^{-1}	0.3 ± 0.04	0.45 ± 0.08
Zn II(2062.66 \AA)	5109.62	1.4772	2.56×10^{-1}	0.7 ± 0.04	0.52 ± 0.09
+Cr II(2062.23 \AA) ^b			7.80×10^{-2}		
Fe II(2382.77 \AA)	5137.88	1.1563	3.01×10^{-1}	0.64 ± 0.08	0.81 ± 0.11
Mg II(2796.35 \AA)	5390.80	0.9278	6.12×10^{-1}	1.04 ± 0.10	1.06 ± 0.13
Mg II(2803.53 \AA)	5403.80	0.9275	3.05×10^{-1}	0.71 ± 0.07	0.91 ± 0.08
Mg I(2852.96 \AA)	5493.01	0.9254	1.83	0.67 ± 0.13	0.63 ± 0.15
Fe II(2600.17 \AA)	5605.97	1.1560	2.24×10^{-1}	1.32 ± 0.07	1.21 ± 0.11
Fe II(2344.21 \AA)	5807.30	1.4773	1.10×10^{-1}	1.97 ± 0.06	1.86 ± 0.06
Fe II(2374.46 \AA)	5881.78	1.4771	3.26×10^{-2}	1.67 ± 0.08	1.80 ± 0.22
Fe II(2382.77 \AA)	5902.60	1.4772	3.01×10^{-1}	2.37 ± 0.09	2.10 ± 0.12
Mg II(2796.35 \AA)	6030.31	1.1565	6.12×10^{-1}	2.07 ± 0.13	2.08 ± 0.16

Table 1. LRIS Line Identifications (Continued)

Line($\lambda_{\text{vac}}(\text{\AA})$)	$\lambda_{\text{helio}}(\text{\AA})$	z	f_{ij}	$W_1(\text{\AA})^c$	$W_2(\text{\AA})^d$
Mg II(2803.53 \AA)	6044.97	1.1562	3.05×10^{-1}	1.77 ± 0.14	1.79 ± 0.15
Mn II(2576.88 \AA)	6383.63	1.4773	3.51×10^{-1}	0.62 ± 0.07	0.50 ± 0.10
Fe II(2586.65 \AA)	6407.39	1.4771	6.84×10^{-2}	1.53 ± 0.08	1.5 ± 0.15
Fe II(2600.17 \AA)	6441.14	1.4772	2.24×10^{-1}	2.48 ± 0.08	2.2 ± 0.13
Mg II(2796.35 \AA)	6926.28	1.4769	6.12×10^{-1}	3.06 ± 0.04	3.00 ± 0.11
Mg II(2803.53 \AA)	6944.62	1.4771	3.05×10^{-1}	2.88 ± 0.04	2.90 ± 0.09
Mg I(2852.96 \AA)	7067.07	1.4771	1.83	1.22 ± 0.05	1.31 ± 0.09

^aAlternative identification to previous entry.

^bDoublet or blend between lines.

^cRest equivalent width on 2001 Feb 22.66.

^dRest equivalent width on 2001 Feb 23.66.

Table 2. ESI Line Identifications

Line($\lambda_{\text{vac}}(\text{\AA})$)	$\lambda_{\text{helio}}(\text{\AA})$	z	f_{ij}	$W_o(\text{\AA})$
Al II(1670.79 \AA)	4138.41	1.47692	1.83	1.87 ± 0.43
Si II(1808.01 \AA)	4478.18	1.47686	2.18×10^{-3}	0.76 ± 0.1
Al III(1854.72 \AA)	4592.39	1.47606	5.60×10^{-1}	0.41 ± 0.20
Fe II(2382.77 \AA) ^a	4592.39	0.92733	3.01×10^{-1}	0.53 ± 0.26
Al III(1854.72 \AA)	4594.04	1.47695	5.60×10^{-1}	0.80 ± 0.18
Fe II(2382.77 \AA) ^a	4594.04	0.92803	3.01×10^{-1}	1.03 ± 0.23
Al III(1862.79 \AA)	4614.18	1.47703	2.79×10^{-1}	0.49 ± 0.07
Fe II(2600.17 \AA)	5011.47	0.92736	2.24×10^{-1}	0.41 ± 0.11
Zn II(2026.14 \AA)	5018.98	1.47711	4.89×10^{-1}	0.91 ± 0.12
+Mg I(2026.48 \AA) ^b			1.15×10^{-1}	
Cr II(2056.25 \AA)	5093.10	1.47689	1.05×10^{-1}	0.44 ± 0.08
Zn II(2062.66 \AA)	5108.62	1.47671	2.56×10^{-1}	0.69 ± 0.16
+Cr II(2062.23 \AA) ^b			7.80×10^{-2}	
Cr II(2066.16 \AA)	5117.54	1.47684	5.15×10^{-2}	0.27 ± 0.12
Fe II(2382.77 \AA)	5138.48	1.15652	3.01×10^{-1}	1.12 ± 0.11
Mg II(2796.35 \AA)	5389.83	0.92745	6.12×10^{-1}	0.96 ± 0.14
Mg II(2803.53 \AA)	5404.04	0.92758	3.05×10^{-1}	1.08 ± 0.16
Mg I(2852.96 \AA)	5498.99	0.92747	1.83	0.51 ± 0.21
Fe II(2260.78 \AA)	5597.47	1.47590	2.44×10^{-3}	0.10 ± 0.08
Fe II(2260.78 \AA)	5599.68	1.47688	2.44×10^{-3}	0.42 ± 0.16
Fe II(2600.17 \AA)	5606.38	1.15616	2.24×10^{-1}	1.15 ± 0.16

Table 2. ESI Line Identification (Continued)

Line($\lambda_{\text{vac}}(\text{\AA})$)	$\lambda_{\text{helio}}(\text{\AA})$	z	f_{ij}	$W_o(\text{\AA})$
Fe II(2344.21 \AA)	5804.03	1.47590	1.10×10^{-1}	0.37 ± 0.11
Fe II(2344.21 \AA)	5806.33	1.47688	1.10×10^{-1}	1.51 ± 0.23
Fe II(2374.46 \AA)	5878.93	1.47590	3.26×10^{-2}	0.30 ± 0.06
Fe II(2374.46 \AA)	5881.25	1.47688	3.26×10^{-2}	1.24 ± 0.10
Fe II(2382.77 \AA)	5899.50	1.47590	3.01×10^{-1}	0.56 ± 0.09
Fe II(2382.77 \AA)	5901.84	1.47688	3.01×10^{-1}	2.21 ± 0.16
Mg II(2796.35 \AA)	6028.98	1.15602	6.12×10^{-1}	2.49 ± 0.08
Mg II(2803.53 \AA)	6044.44	1.15601	3.05×10^{-1}	2.14 ± 0.60
Mg I(2852.96 \AA)	6152.90	1.15667	1.83	0.54 ± 0.31
Mn II(2576.88 \AA)	6382.58	1.47686	3.51×10^{-1}	0.58 ± 0.12
Fe II(2586.65 \AA)	6404.29	1.47590	6.84×10^{-2}	0.64 ± 0.13
Fe II(2586.65 \AA)	6406.82	1.47688	6.84×10^{-2}	1.72 ± 0.20
Mn II(2594.50 \AA)	6426.18	1.47685	2.71×10^{-1}	0.68 ± 0.12
Fe II(2600.17 \AA)	6437.76	1.47590	2.24×10^{-1}	0.49 ± 0.05
Fe II(2600.17 \AA)	6440.31	1.47688	2.24×10^{-1}	2.12 ± 0.19
Mn II(2606.46 \AA)	6455.96	1.47691	1.93×10^{-1}	0.56 ± 0.12
Mg II(2796.35 \AA)	6923.66	1.47596	6.12×10^{-1}	1.63 ± 0.24
Mg II(2796.35 \AA)	6926.76	1.47707	6.12×10^{-1}	1.51 ± 0.19
Mg II(2803.53 \AA)	6940.97	1.47580	3.05×10^{-1}	1.39 ± 0.15
Mg II(2803.53 \AA)	6944.06	1.47690	3.05×10^{-1}	1.61 ± 0.11
Mg I(2852.96 \AA)	7063.74	1.47593	1.83	0.42 ± 0.24
Mg I(2852.96 \AA)	7066.33	1.47684	1.83	1.21 ± 0.22

^aAlternative identification to previous entry.

^bDoublet or blend between lines.

Table 3. Derived Column Densities for the z_{1b} System

Ion(j)	$\lambda_{\text{vac}}(\text{\AA})$	f_{ij}	b (km s $^{-1}$)	$\log(N_j)$	$\log(N_{\text{HI}})^{\text{a}}$	$\log(N_{\text{HI}})_{\text{corr}}^{\text{b}}$	$[\text{Zn}/J]^{\text{c}}$
Mn $^{+}$	2576.88	0.3508	22.8	14.00 ± 0.44	20.47 ± 0.44	21.92 ± 0.44	0.50
	2594.50	0.2710	35.3	13.95 ± 0.17	20.42 ± 0.17	21.87 ± 0.18	
	2606.46	0.1927	29.6	14.00 ± 0.20	20.47 ± 0.20	21.92 ± 0.21	
Mg $^{+}$	2803.53	3.05×10^{-1}	. . .	$\geq 13.88^{\text{d}}$	≥ 18.30	≥ 19.85	≤ 2.65
Fe $^{+}$	2382.77	3.01×10^{-1}	. . .	$\geq 14.16^{\text{d}}$	≥ 18.65	≥ 20.92	≤ 2.3

^aAssuming solar abundances and no depletion.

^bAssuming depletion corrections from Savage & Sembach (1996).

^cAverage log metal abundance ratio relative to Solar value.

^dUsing Equation (3).

Table 4. Column Densities for Blended Lines

Ion(j)	$\log(N_j)$	$\log(N_{\text{HI}})^{\text{a}}$	$\log(N_{\text{HI}})_{\text{corr}}^{\text{b}}$	$[\text{Zn}/J]^{\text{c}}$
Zn ⁺	13.60 ± 0.07	21.04 ± 0.07	21.71 ± 0.07	. . .
Cr ⁺	14.02 ± 0.1	20.37 ± 0.1	22.65 ± 0.1	0.61

^aAssuming solar abundances and no depletion.

^bAssuming depletion corrections from Savage & Sembach (1996).

^cLog metal abundance ratio relative to Solar value.

Table 5. Photoionization Model Parameters

$N_{\text{HI}}(\text{cm}^{-2})$	$n_{\text{HI}}(\text{cm}^{-3})$	$r_{\text{max}}(\text{pc})$	Model
$10^{20.44}$	0.089	1000.0	I
$10^{20.44}$	0.89	100.0	II
$10^{20.44}$	89	1.0	III
$10^{20.44}$	2.75×10^3	6.48×10^{-2}	IV
$10^{22.00}$	3.2	1000.0	V
$10^{22.00}$	2.0×10^4	0.19	VI
$10^{22.00}$	10^5	6.48×10^{-2}	VII
$10^{22.00}$	10^6	3.56×10^{-2}	VIII

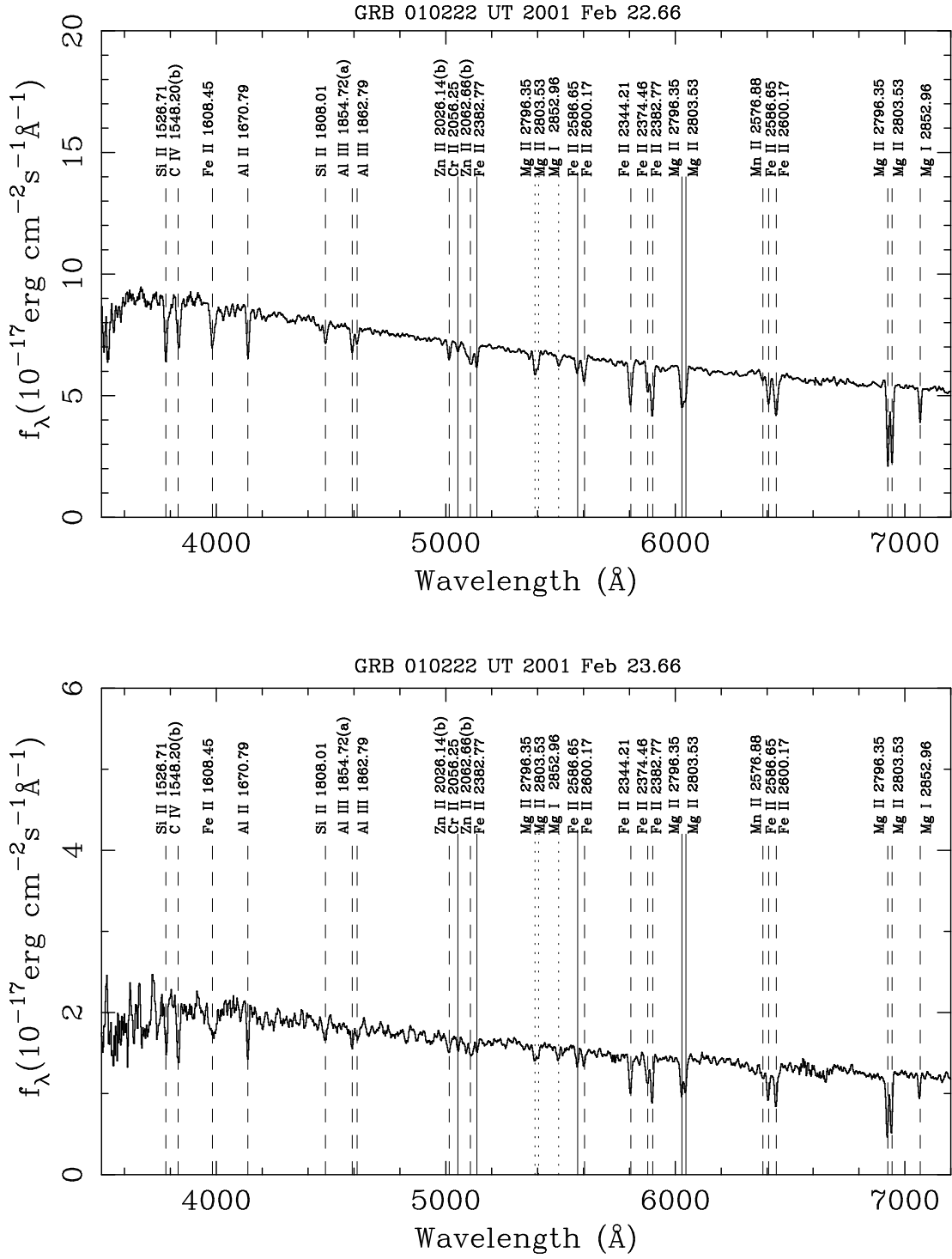


Fig. 1.— LRIS spectra of GRB 010222 on 2001 Feb. 22.66 and Feb 23.66 corrected for Galactic foreground extinction and smoothed with a boxcar corresponding to the instrumental resolution. Three absorption systems are labelled: $z_1 = 1.47688$ (*dashed lines*), $z_2 = 1.15628$ (*solid lines*), and $z_3 = 0.92747$ (*dotted lines*). Letters in parentheses refer to the notes in Table 1.

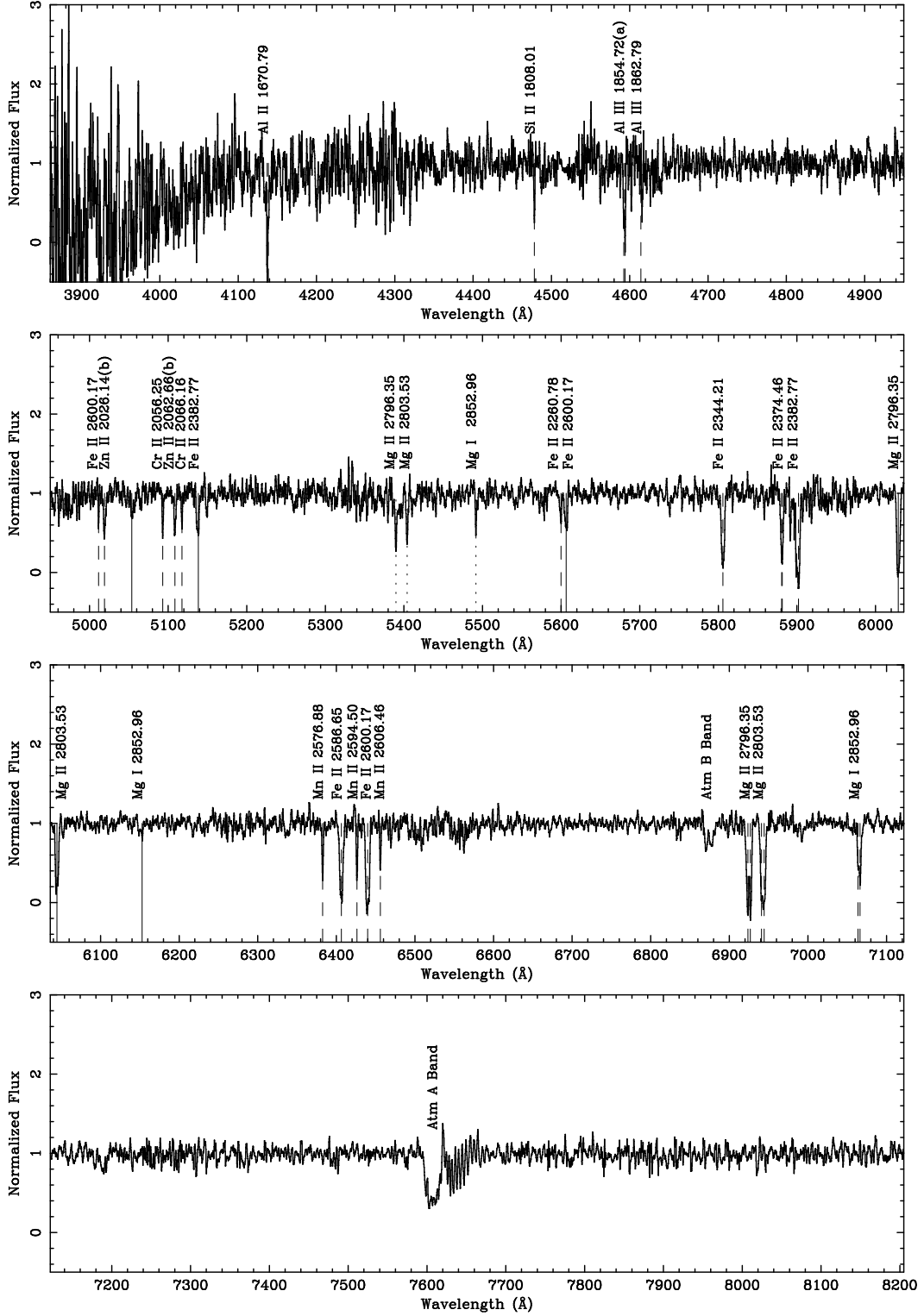


Fig. 2.— Continuum-normalized ESI spectrum of GRB 010222 on 2001 Feb. 23.61. The spectrum is smoothed with a boxcar corresponding to the instrumental resolution. Three absorption systems are labelled: $z_1 = 1.47688$ (*dashed lines*), $z_2 = 1.15628$ (*solid lines*), and $z_3 = 0.92747$ (*dotted lines*). Atmospheric bands are also indicated. Letters in parentheses refer to the notes in Table 2.

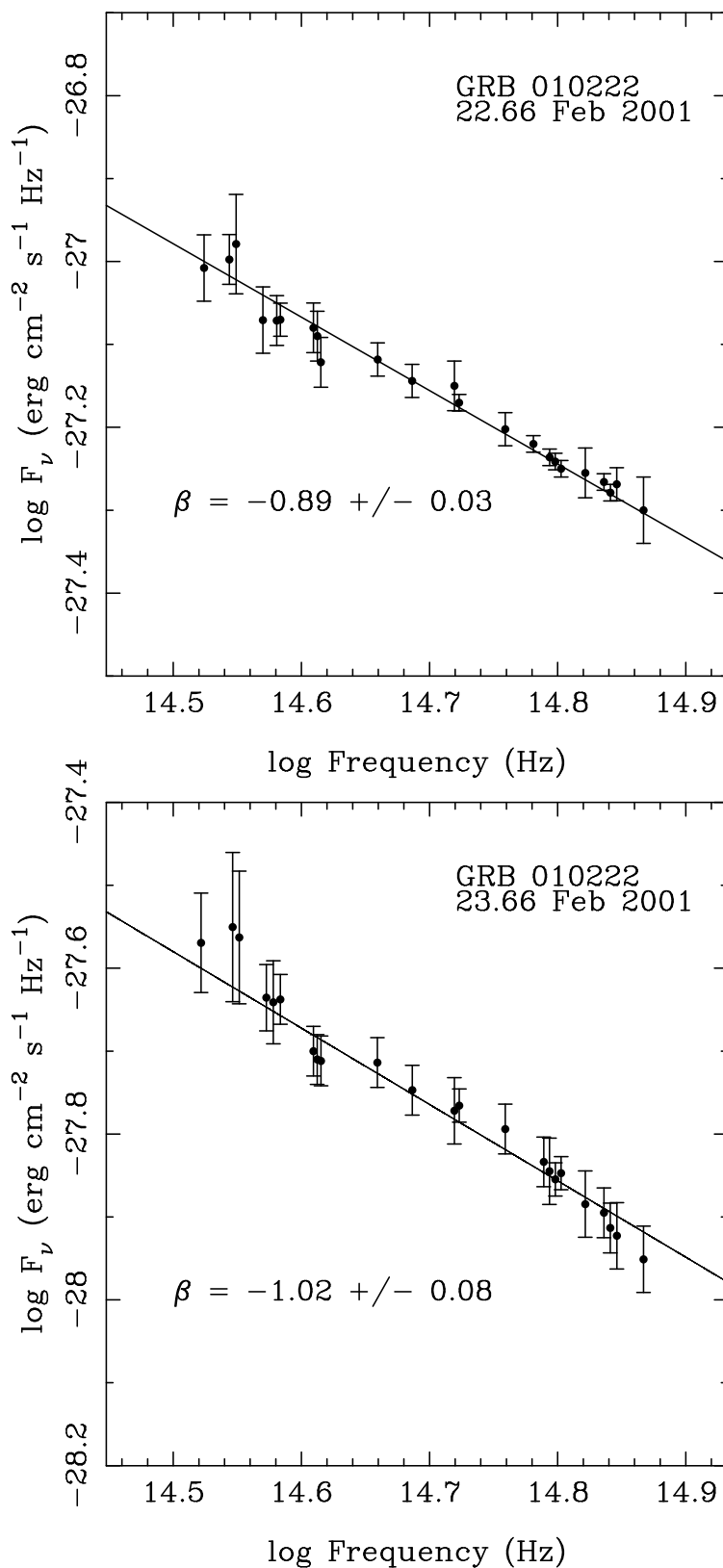


Fig. 3.— Optical continuum points with 1σ standard deviation uncertainties, along with the best fitted line that minimizes χ^2 , for 2001 Feb 22.66 and 2001 Feb 23.66.

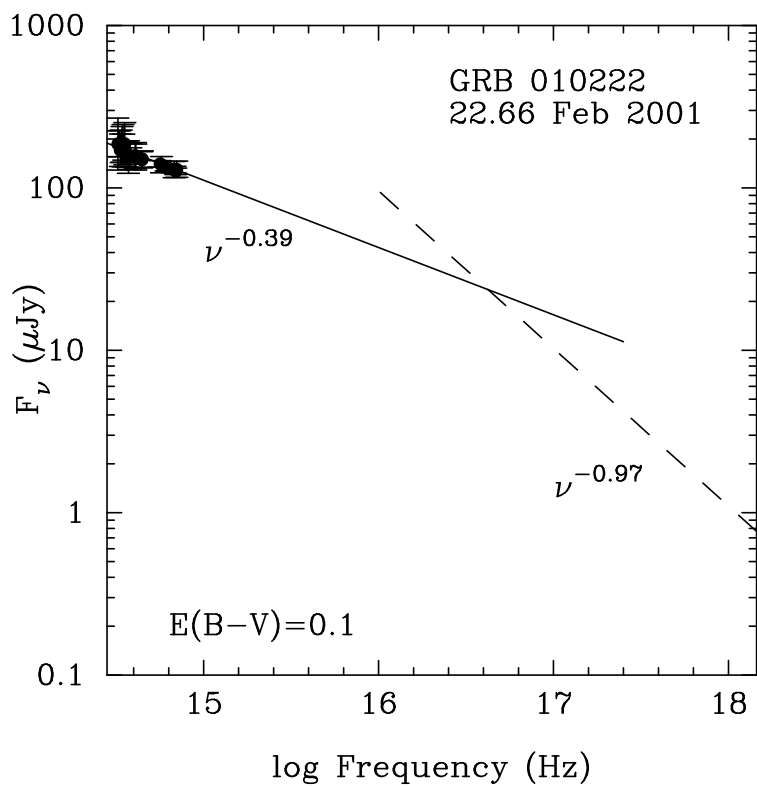


Fig. 4.— Multiwavelength X-ray and optical continuum corrected for dust using the extinction curve of Calzetti et al. (2000) and color excess $E(B - V) = 0.1$ for 2001 Feb 22.66. The resulting optical spectrum has a slope $\beta \approx -0.43$. The X-ray data is shown schematically as a *dashed line*, while the best fit through the optical data is plotted as a *solid line*.

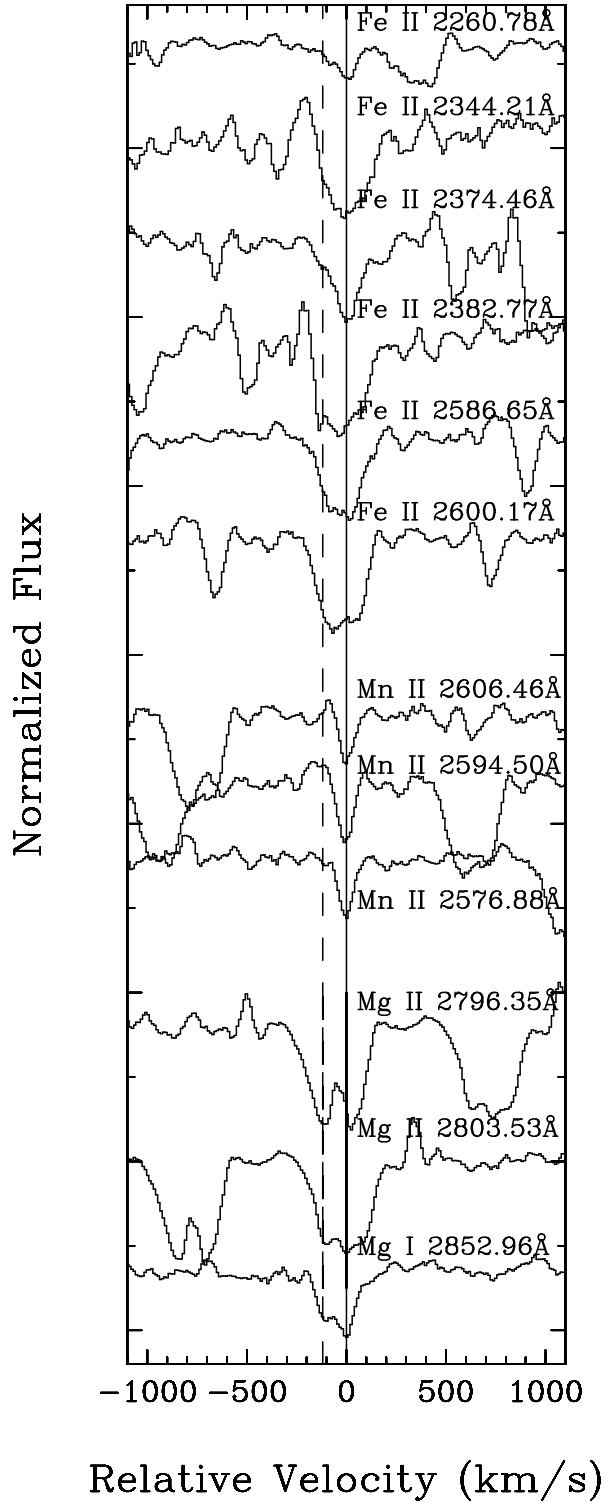


Fig. 5.— Metallic absorption-line profiles in the ESI spectrum plotted in velocity space, showing evidence of substructure in the most distant absorber(z_1). As zero velocity we use the systemic redshift, $z = 1.47688$. The *dashed line* indicates the average offset of $v = -119$ km s $^{-1}$ from the systemic velocity.

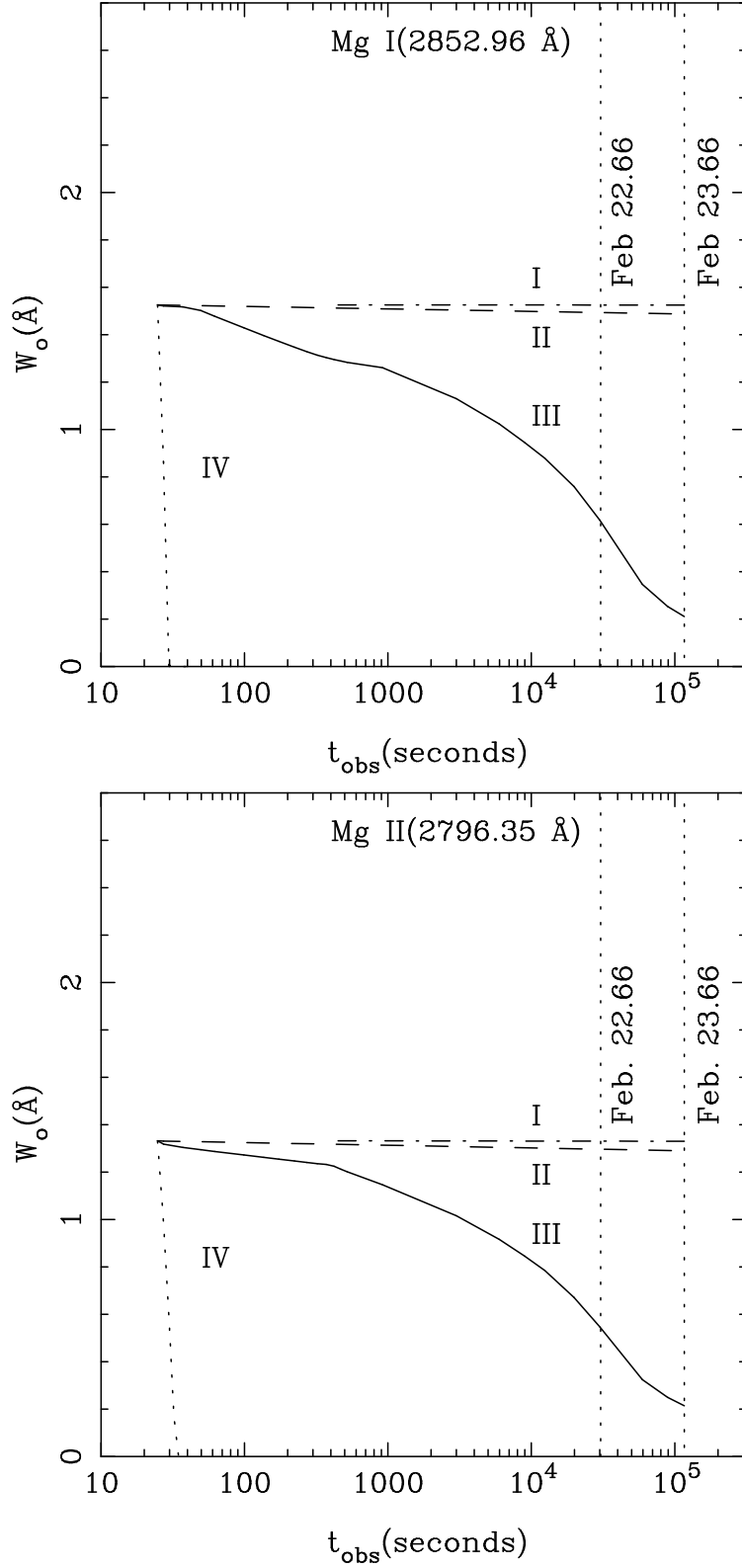


Fig. 6.— Modelled time evolution of the Mg I (2852.96 Å) and Mg II (2796.35 Å) equivalent widths for different sets of initial conditions (Table 5), constrained by ($N_{\text{HI}} = 10^{20.44} \text{ cm}^{-2}$).

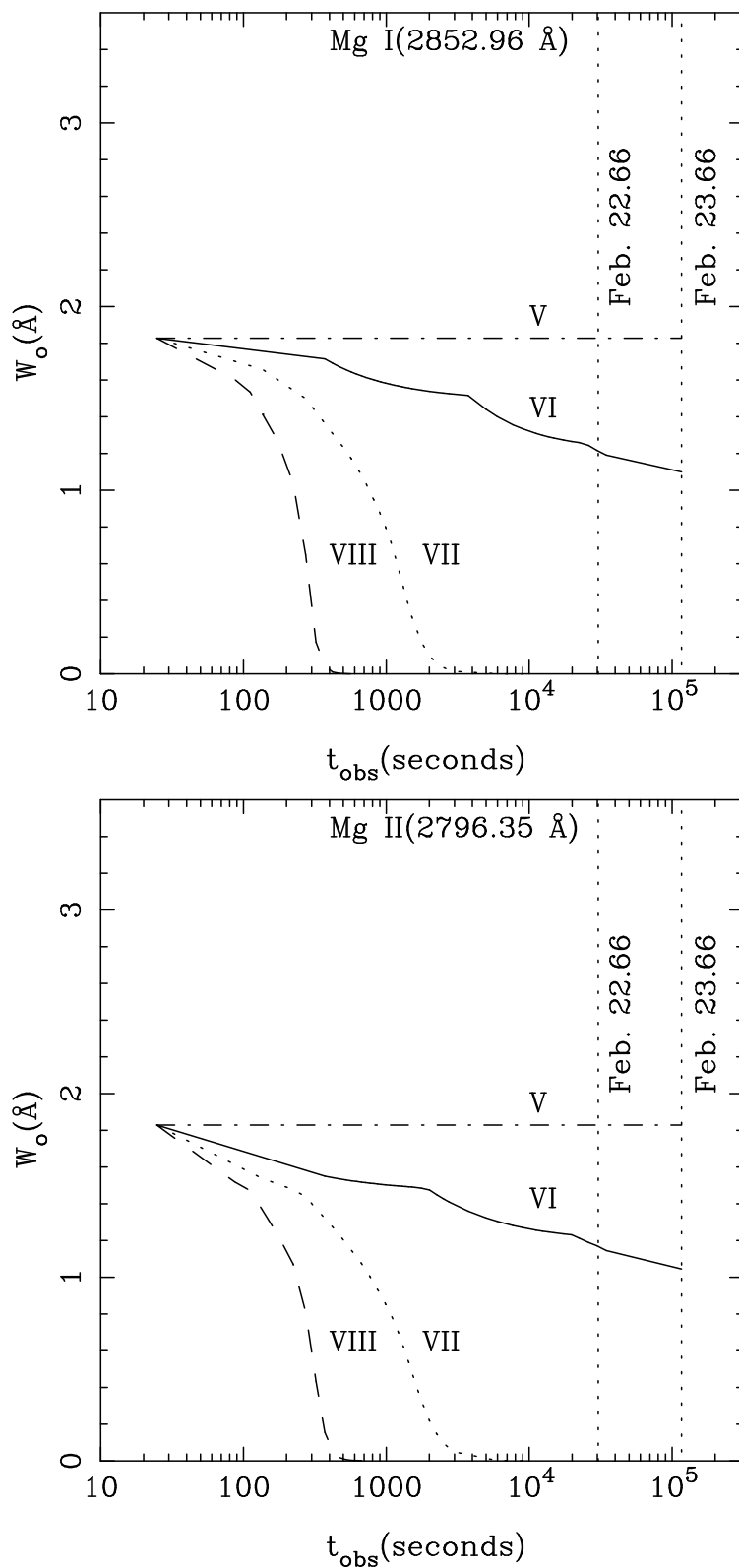


Fig. 7.— Modelled time evolution of the Mg I (2852.96 Å) and Mg I (2796.35 Å) equivalent widths for different sets of initial conditions (Table 5), constrained by ($N_{\text{HI}} = 10^{22} \text{ cm}^{-2}$).